Marine anoxia and delayed Earth system recovery after the end-Permian extinction

Kimberly V. Lau[a,1], Kate Maher[a], Demir Altiner[b], Brian M. Kelley[a,2], Lee R. Kump[c], Daniel J. Lehrmann[d], Juan Carlos Silva-Tamayo[e], Karrie L. Weaver[a], Meiyi Yu[f], and Jonathan L. Payne[a]

[a]Department of Geological Sciences, Stanford University, Stanford, CA 94305; [b]Department of Geological Engineering, Middle East Technical University, 06531 Ankara, Turkey; [c]Department of Geosciences, The Pennsylvania State University, University Park, PA 16802; [d]Geosciences Department, Trinity University, San Antonio, TX 78212; [e]Department of Earth and Atmospheric Sciences, University of Houston, Houston, TX 77204; and [f]College of Resource and Environment Engineering, Guizhou University, 550003 Guizhou, China

Edited by Paul F. Hoffman, University of Victoria, Victoria, British Columbia, Canada, and approved January 8, 2016 (received for review August 1, 2015)

Delayed Earth system recovery following the end-Permian mass extinction is often attributed to severe ocean anoxia. However, the extent and duration of Early Triassic anoxia remains poorly constrained. Here we use paired records of uranium concentrations ([U]) and $^{238}U/^{235}U$ isotopic compositions ($\delta^{238}U$) of Upper Permian–Upper Triassic marine limestones from China and Turkey to quantify variations in global seafloor redox conditions. We observe abrupt decreases in [U] and $\delta^{238}U$ across the end-Permian extinction horizon, from ∼3 ppm and −0.15‰ to ∼0.3 ppm and −0.77‰, followed by a gradual return to preextinction values over the subsequent 5 million years. These trends imply a factor of 100 increase in the extent of seafloor anoxia and suggest the presence of a shallow oxygen minimum zone (OMZ) that inhibited the recovery of benthic animal diversity and marine ecosystem function. We hypothesize that in the Early Triassic oceans—characterized by prolonged shallow anoxia that may have impinged onto continental shelves—global biogeochemical cycles and marine ecosystem structure became more sensitive to variation in the position of the OMZ. Under this hypothesis, the Middle Triassic decline in bottom water anoxia, stabilization of biogeochemical cycles, and diversification of marine animals together reflect the development of a deeper and less extensive OMZ, which regulated Earth system recovery following the end-Permian catastrophe.

paleoredox | uranium isotopes | biogeochemical cycling | carbon isotopes | Early Triassic

The end-Permian mass extinction—the most severe biotic crisis in the history of animal life—was followed by 5 million years of reduced biodiversity (1, 2), limited ecosystem complexity (3), and large perturbations in global biogeochemical cycling (4, 5). Ocean anoxia has long been invoked both as a cause of the extinction (6–8) and as a barrier to rediversification (9). Numerous lines of evidence demonstrate widespread anoxic conditions around the time of the end-Permian mass extinction (e.g., refs. 6 and 10–12). In contrast, the prevalence of anoxia during the 5- to 10-million-year recovery interval remains poorly constrained (13, 14).

Reconstructing paleoredox conditions is challenging because some indicators of anoxia characterize only the local conditions of the overlying water column, whereas other indicators may be influenced by confounding factors, such as weathering rates on land. Here, we use paired measurements of [U] and $\delta^{238}U$ in marine carbonate rocks to differentiate changes in weathering of U from variations in global marine redox conditions. Microbially mediated reduction of U(VI) to U(IV) under anoxic conditions at the sediment–water interface results in a substantial decrease in uranium solubility and a measureable change in $^{238}U/^{235}U$ (15–18). Because ^{238}U is preferentially reduced and immobilized relative to ^{235}U, the $\delta^{238}U$ value of seawater U(VI) decreases as the areal extent of bottom water anoxia increases (Fig. S1). Consequently, a global increase in the extent of anoxic bottom waters will cause simultaneous decreases in [U] and $\delta^{238}U$ of carbonate sediments. A previous study of $\delta^{238}U$ variations at one stratigraphic section through the immediate extinction interval (∼40,000 y) (11) suggested a rapid onset of anoxia coincident with the loss of marine diversity. However, with only a single site, it is unclear if the signal is globally representative; moreover, the lack of data for all but the lowest biostratigraphic zone of the Triassic leaves the pattern and timing of environmental amelioration during the recovery interval unconstrained.

To develop a quantitative, global reconstruction of seawater redox conditions for the entire 15-million-year interval of mass extinction and subsequent Earth system recovery, we measured 58 Upper Permian (Changhsingian) through Upper Triassic (Carnian) limestone samples from three stratigraphic sections (Dajiang, Dawen, and Guandao) arrayed along a depth transect on the Great Bank of Guizhou (GBG), an isolated carbonate platform in the Nanpanjiang Basin of south China (eastern Tethys). To test the extent to which variations in [U] and $\delta^{238}U$ within the GBG reflect global uranium cycling, we also analyzed 28 limestone samples from the Taşkent section, Aladag Nappe, Turkey, located in the western Tethys (Fig. S1). We focused our measurements on samples deposited in shallow marine environments (<100 m water depth, i.e., Dajiang, Dawen, and Taşkent) likely to have remained oxygenated. Variations in [U] and $\delta^{238}U$ in these samples should reflect changes in global, rather than local, redox conditions.

Significance

The end-Permian mass extinction not only decimated taxonomic diversity but also disrupted the functioning of global ecosystems and the stability of biogeochemical cycles. Explaining the 5-million-year delay between the mass extinction and Earth system recovery remains a fundamental challenge in both the Earth and biological sciences. We use coupled records of uranium concentrations and isotopic compositions to constrain global marine redox conditions across the end-Permian extinction horizon and through the subsequent 17 million years of Earth system recovery. Our finding that the trajectory of biological and biogeochemical recovery corresponds to variations in an ocean characterized by extensive, shallow marine anoxia provides, to our knowledge, the first unified explanation for these observations.

Author contributions: K.V.L., K.M., and J.L.P. designed research; K.V.L. performed research; K.V.L., K.M., L.R.K., and J.L.P. analyzed data; K.V.L., K.M., D.A., L.R.K., D.J.L., J.C.S.-T., K.L.W., and J.L.P. wrote the paper; D.A., B.M.K., D.J.L., and M.Y. provided samples and stratigraphic data; L.R.K. contributed to data interpretation and modeling; and J.C.S.-T. contributed to data interpretation.

The authors declare no conflict of interest.

This article is a PNAS Direct Submission.

Freely available online through the PNAS open access option.

[1]To whom correspondence should be addressed. Email: kvlau@stanford.edu.

[2]Present address: ExxonMobil Upstream Research Company, Houston TX 77389.

This article contains supporting information online at www.pnas.org/lookup/suppl/doi:10.1073/pnas.1515080113/-/DCSupplemental.

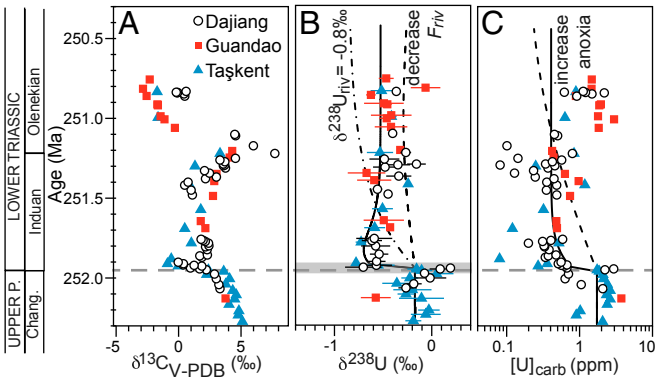

Fig. 1. Late Permian (P.) to early Early Triassic (*A*) $\delta^{13}C$, (*B*) $\delta^{238}U$, and (*C*) [U] data and box model results. Gray dashed line indicates end-Permian extinction horizon. Shaded box in *B* represents the temporal extent of data reported in ref. 11. Model results are as follows: increased extent of anoxia (f_{anox}) from modern value of 0.2% to 20% for the first ~30,000 y and to 5% thereafter (solid line); decreased input [U] by an order of magnitude (dashed line); and decreased input $\delta^{238}U$ value to –0.8‰ (dot-dashed line). The $\delta^{13}C$ data are from ref. 4 (Dajiang and Guandao) and this study (Taşkent). Error bars on $\delta^{238}U$ are 2σ of replicate analyses and are reported relative to CRM-145. Data from Dawen are shown in Fig. S2, and details of age model are shown in Figs. S2–S4. Chang., Changhsingian.

Results

The $\delta^{238}U$ composition of the shallow marine sections averages –0.15‰ in the Upper Permian and abruptly decreases at the extinction horizon to a minimum value of –0.77‰ (Fig. 1, Figs. S2–S4, and Dataset S1). Synchronously, [U] decreases from 3 ppm to ~0.3 ppm. In the Induan strata, representing the first ~0.7 My after the extinction, [U] and $\delta^{238}U$ values remain low (0.4 ppm and –0.55‰) in both shallow marine (Dajiang and Taşkent) and slope (Guandao) environments. Lowermost Induan $\delta^{238}U$ data from Dawen have a mean of –0.57‰ (Fig. S2). In the Olenekian strata, representing the subsequent ~4 My, [U] and $\delta^{238}U$ values gradually increase to 1 ppm and ~0.35‰ (Fig. 2). In the uppermost Olenekian strata (~247.5 Ma), [U] and $\delta^{238}U$ decrease to 0.6 ppm and –0.65‰ at Guandao and Taşkent (Dajiang strata are dolomitized and are not considered). In limestones above the Olenekian–Anisian boundary (~247 Ma), [U] and $\delta^{238}U$ increase to 1.2 ppm and –0.23‰.

Three lines of evidence indicate that these general trends in [U] and $\delta^{238}U$ reflect secular changes in global seawater redox conditions rather than local or diagenetic effects. First, shallow marine uranium records exhibit consistent trends and similar absolute values between China and Turkey, despite vast differences in geographic settings and burial histories. In our records, differences in [U] and $\delta^{238}U$ across time intervals are statistically significant both within individual stratigraphic sections and across the entire dataset, whereas the values between sections are statistically indistinguishable (Table S1 and *Statistical Analysis: Interpretation*). Local or diagenetic controls would likely produce differences among sites rather than differences expressed across time. Second, our uranium data are not significantly correlated with indicators of diagenetic alteration such as $\delta^{18}O$, Mn/Sr, Mg/Ca, or organic carbon content, and do not covary with proxies for detrital contribution (normalization with Al or Th) or indictors of mineralogy (Sr/Ca) (Fig. S5 and *Diagenetic Alteration and Dolomitization* and *Statistical Analysis: Interpretation*).

Finally, the trends in [U] from our stratigraphic sections agree with published records from shallow marine carbonates spanning the Permian–Triassic boundary interval in Saudi Arabia, Iran, Italy, and China (8, 11–13, 26, 27). Although local and diagenetic processes affect all samples of this age and undoubtedly account for some of the variation in our dataset, the most parsimonious explanation for the statistically supported trends in [U] and $\delta^{238}U$ is that the dominant signal in the dataset is a primary signature reflecting the uranium composition of seawater.

Discussion

Statistically Significant Temporal Trends. To determine whether the temporal trends we observe in $\delta^{238}U$ and [U] are statistically significant, we used analysis of variance (ANOVA) (function *aov* in R) for our data categorized by general time intervals (Late Permian, Induan, Olenekian, and Middle–Late Triassic) (Table S1). Both [U] and $\delta^{238}U$ data from shallow marine records differ significantly among time intervals (P values ≤ 0.01). We then used Dennett's modified Tukey–Kramer Post-Hoc Test (function *DTK.test* in R) to run pair-wise comparisons between time intervals for all our data. The results for the combined dataset show that for both [U] and $\delta^{238}U$, the Induan is significantly different from the Late Permian, Olenekian, and Middle–Late Triassic compositions (Fig. 3).

In addition, we applied one-way ANOVA and Dennett's modified Tukey–Kramer Post-Hoc test to the [U] and $\delta^{238}U$ records for the shallow marine stratigraphic sections (Table S1). For both Dajiang and Taşkent, the Induan $\delta^{238}U$ values are significantly different from the Late Permian and Middle–Late Triassic, whereas [U] values are only significantly different between the Induan and the Middle–Late Triassic for Taşkent. The results from Dawen (combined with data from ref. 11) also indicate a significant difference between the Late Permian and Induan $\delta^{238}U$ data. However, the Olenekian [U] and $\delta^{238}U$ results are not consistent, and differ in whether or not they are significantly distinguishable from the Induan (Taşkent) or not (Dajiang).

In contrast, data from Guandao did not show significant differences between the various time intervals, suggesting that Guandao sediments on the platform slope may have been impacted by local anoxia/suboxia. These conditions could result in locally more negative $\delta^{238}U$ if a greater proportion of ^{238}U relative to seawater was reduced into proximally deposited sediments, which would not be captured in our measurements. Therefore, the presence of local anoxia may result in $\delta^{238}U$ compositions that deviate from global seawater.

From these statistical results, we conclude that the Induan had significantly lower [U] and $\delta^{238}U$ values than the uppermost Permian and the Middle–Upper Triassic at all sites, whereas the Olenekian is a transitional period. The uppermost Permian and Middle–Upper Triassic data are statistically indistinguishable, implying a recovery in [U] and $\delta^{238}U$ to preextinction values.

Modeling Implications for Seafloor Anoxia. A mass balance box model of seawater uranium and its isotopes (Fig. 1 and Fig. S6) demonstrates that the observed decreases in [U] and $\delta^{238}U$ require an increase in bottom water anoxia in the global ocean. Scenarios involving a decrease in either [U] or $\delta^{238}U$ of riverine uranium would account for a decrease in one metric but not both. Even simultaneous decreases in riverine [U] and $\delta^{238}U$ would not reproduce the rapid observed decreases (Fig. S6). In contrast, expanding the area of seafloor impacted by anoxia efficiently removes and fractionates U, causing large, rapid, and sustained decreases in [U] and $\delta^{238}U$, consistent with the magnitude and rate of change of the negative shifts in [U] and $\delta^{238}U$ at the extinction horizon.

The extent of Early Triassic anoxia implied by our box model calculations is substantial. Our model predicts an increase in the anoxic sink for uranium from 15% of the total removal flux in the latest Permian to 94% in the Induan, similar to the factor of 6 increase in the flux of U to anoxic facies calculated in ref. 11. However, the magnitude and rate of decrease in [U] and $\delta^{238}U$ also require a factor of 100 increase in the extent of seafloor anoxia (f_{anox}) across the extinction horizon, from 0.2% (28) to 20% of the seafloor during the extinction interval, followed by a

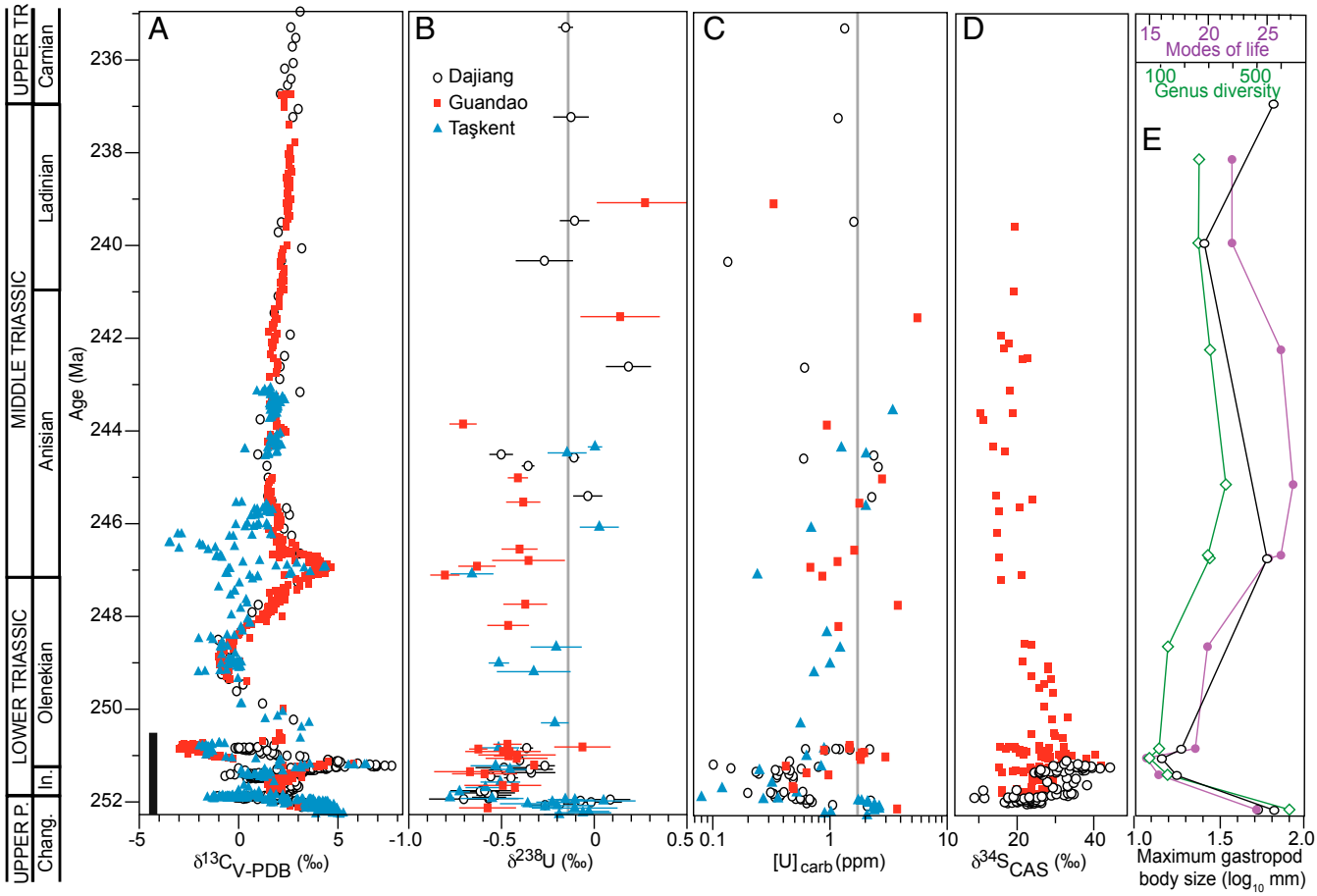

Fig. 2. Late Permian (P.) to Late Triassic (Tr.) [U] and $\delta^{238}U$ data and global records of biogeochemical cycling and biotic recovery. (*A*) The $\delta^{13}C$ data are from ref. 4 (Dajiang and Guandao) and this study (Taşkent). Vertical black bar depicts temporal extent of $\delta^{238}U$ data from Fig. 1. (*B*) The $\delta^{238}U$ data. Error bars on $\delta^{238}U$ data are 2σ of replicate analyses and are reported relative to CRM-145. (*C*) [U] data. Vertical gray lines in *B* and *C* are the mean Late Permian values. (*D*) Carbonate-associated sulfate sulfur isotope data ($\delta^{34}S_{CAS}$) (5). (*E*) Global trends in sampled-in-bin genus diversity (green open diamonds) (3), modes of life (purple circles) (3), and maximum gastropod body size (black open circles) (25). The age model is based on geochronology (23, 24), biostratigraphy, and chemostratigraphy (details are shown in Figs. S2–S4). Chang., Changhsingian; In., Induan.

1.5-My interval during which 5% of the seafloor was anoxic (Figs. 1 and 3 and Fig. S6). During the rest of the Olenekian, 1% of the seafloor may have remained anoxic, still a fivefold increase over preextinction conditions (Fig. 3). Collectively, these findings indicate persistent and gradually decreasing anoxia for the 5 million years following the end-Permian mass extinction, followed by a return to preextinction conditions that are more positive than modern seawater composition (*Middle Triassic $\delta^{238}U$ Composition*).

Anoxia and Earth System Recovery. In the modern ocean, continental shelves comprise ∼7% of the seafloor area but host a disproportionate share of marine animal diversity, biomass, and the burial of biogeochemically important elements (e.g., carbon and sulfur). Our uranium data, combined with biomarker support for photic-zone euxinia (6) and petrographic, geochemical, and modeling evidence for an expanded oxygen minimum zone (OMZ) rather than deep-ocean anoxia (20, 29–31), indicate that anoxic waters may have bathed a large fraction of Early Triassic outer continental shelves and upper slopes in anoxic waters. These conditions could explain the limited diversity and ecological complexity of marine ecosystems (3), as well as the reduced maximum and mean body sizes of benthic animals (25).

Given the nonlinear hypsometry of the continental margin, fluctuations in the depth of the upper boundary of the OMZ could strongly influence the burial of reduced versus oxidized forms of carbon and sulfur, offering a potential explanation for the biogeochemical anomalies of the Early Triassic. For example, in the presence of a shallow OMZ, the area of seafloor covered by anoxic waters is sensitive to episodic expansion of the OMZ or variations in eustatic sea level (Fig. 4*A* and Fig. S7). Specifically, intervals of vertical expansion of the OMZ, or high sea level and extensive continental flooding, would be associated with expanding anoxic bottom waters. Consequently, the extent of seafloor anoxia (f_{anox}) and the rate of organic carbon burial would covary with the depth of the upper boundary of the OMZ relative to the shelf–slope break (Z_{UB}), potentially causing large $\delta^{13}C$ excursions. Under this scenario, associated increases in pyrite burial would increase the $\delta^{34}S$ of carbonate-associated sulfate ($\delta^{34}S_{CAS}$), reduce the size of the sulfate reservoir, and promote conditions for $\delta^{34}S_{CAS}$ instability (5, 32).

To test the potential for variations in Z_{UB} to influence global carbon cycling, we constructed a box model of the geologic carbon cycle, modified from ref. 33 (*Modeling the Effect of a Shallow OMZ*). In the model, the magnitude of $\delta^{13}C$ response to the same forcing can vary substantially depending upon the depth of the OMZ (Fig. 4*C*). Based upon our uranium data, we simulated a scenario in which the upper boundary of the OMZ deepens gradually across Early Triassic time while the frequency of oscillations in Z_{UB} decreases (Fig. S8). By varying these two simple controls, we are able to reproduce the general behavior of the

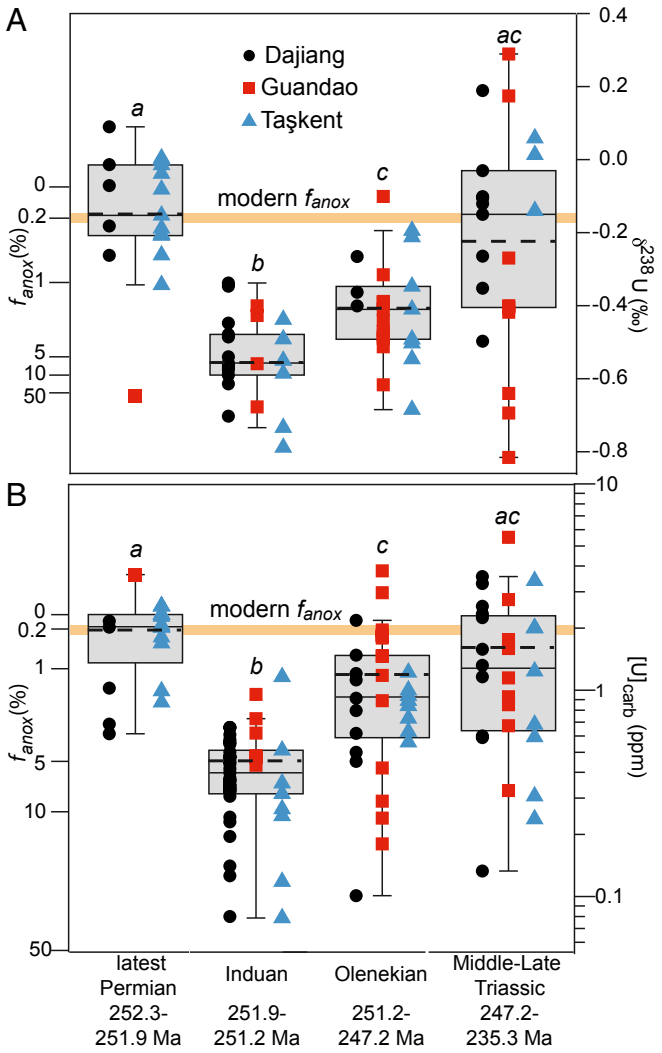

Fig. 3. (*A*) The δ^{238}U and (*B*) [U] boxplots. Whiskers denote the minimum and maximum of data within 1.5 times the interquartile range from the median. The mean is marked by the dashed line. Steady-state model predictions for the extent of anoxia, f_{anox}, are calculated for the best-estimate input $\delta^{238}U_{riv}$ composition of −0.05‰ (*Middle Trassic δ^{238}U Composition*), and suggest that, in the Late Permian and Late–Middle Triassic, the extent of anoxia was near the modern value, whereas, in the Early Triassic, the extent was larger. Statistical analyses show that latest Permian δ^{238}U and [U] data (*a*) are significantly distinct from the Induan (*b*) but similar to the Middle–Late Triassic, whereas the Olenekian data represent a transitional period (*c*).

Early–Middle Triassic carbon cycle, with large, rapid excursions giving way to smaller and more prolonged variations. Importantly, we are able to produce the δ^{13}C excursions without varying the magnitude of the forcing (variation in Z_{UB}) or requiring any large external perturbation to the Earth system. This effect could account for the magnitude and persistence of Early Triassic δ^{13}C and δ^{34}S excursions after the initial negative excursion associated with Siberian Traps volcanism (4, 5, 32) (Fig. 2).

In summary, uranium data confirm a central role for marine redox conditions in modulating Earth system recovery following the end-Permian extinction. The return of marine redox conditions to a preextinction state in the Middle Triassic was concurrent with stabilization of δ^{13}C and $\delta^{34}S_{CAS}$ values and a return to baseline genus richness, ecological diversity, and animal body size (2, 3, 25). We propose that, as the redox gradient in the upper few hundred meters of the water column diminished due to a deepening of the OMZ and, perhaps, a reduction in total primary productivity (e.g., ref. 20), benthic communities recovered, and the sensitivity of organic carbon burial to subsequent variations decreased, stabilizing the global carbon and sulfur cycles (Fig. 4). Combined with the long-term trend of increasing seawater oxygenation during the Phanerozoic, long-term deepening of the OMZ and an associated decrease in the sensitivity of global biogeochemical cycles may also explain the trends toward greater taxonomic diversity and ecological complexity, as well as the reduced frequency of large carbon and sulfur isotope anomalies.

Materials and Methods

Uranium Box Model. In the modern ocean, where the extent of anoxia is small (~0.2%) (28) relative to conditions over most of Earth's history, seawater δ^{238}U is invariant at about −0.4‰ (15–17). If carbonates faithfully record seawater chemistry with no postdepositional effects (refs. 15–17 and 34, but see further discussion in ref. 34), then the δ^{238}U of carbonates should decrease as regions of anoxic marine bottom waters expand. Because uranium has a residence time (3.2–5.6 × 10^5 y) (35) significantly longer than ocean mixing time (10^3 y), global seawater variations in [U] and δ^{238}U should be reflected within local sediments.

The unique sensitivity of both δ^{238}U and uranium concentrations to the extent of bottom water anoxia can be described by differential mass balance equations for the seawater uranium inventory and its isotopic composition, respectively,

$$\frac{dN_{sw}}{dt} = J_{riv} - J_{anox} - J_{other} \quad [1]$$

$$\frac{N_{sw} * d\delta^{238}U}{dt} = J_{riv} * \left(\delta^{238}U_{riv} - \delta^{238}U\right) - J_{anox} * \Delta_{anox} - J_{other} * \Delta_{other} \quad [2]$$

where N_{sw} is the oceanic uranium inventory in moles, $\delta^{238}U$ is the value of seawater, $\delta^{238}U_{riv}$ is the value of the riverine source, Δ_{anox} = +0.6‰ is the effective fractionation factor associated with anoxic sediment deposition (17), and Δ_{other} is the effective fractionation factor associated with the remaining other sinks [+0.03‰, calculated to maintain isotopic steady state in the modern ocean (e.g., refs. 11 and 36)]. We simplify the inputs to J_{riv}, the riverine flux [modern value is 0.4 × 10^8 mol U/y (37)]. The outputs are assumed to consist of the anoxic sediment sink (J_{anox}) and the sum of the other

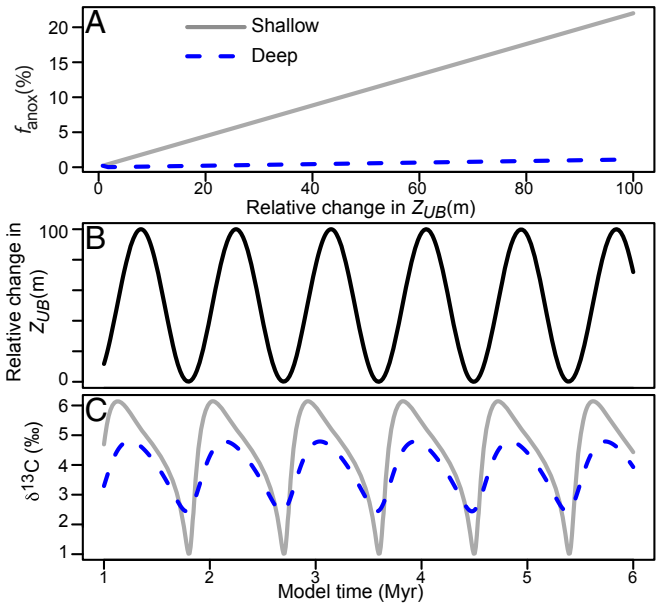

Fig. 4. Sensitivity of δ^{13}C to changes in the depth of the upper boundary of the OMZ, Z_{UB}. (*A*) Relationship between f_{anox} and the depth of the upper boundary of the OMZ relative to the continental shelf–slope break, Z_{UB}, for scenarios with a shallow OMZ (gray line) and deep OMZ (dashed blue line). (*B*) Temporal change in Z_{UB} used in model. (*C*) Model output for δ^{13}C. Model results are shown starting at 1 My, after the system has reached a quasi-steady state. Refer to *Supporting Information* for model details.

sinks (J_{other}), where $J_{anox} = 0.06 \times 10^8$ mol U/y (37) and J_{other} is calculated by mass balance to an initial steady-state value of 0.34×10^8 mol U/y. We further define the output flux terms J_{anox} and J_{other} as

$$J_{anox} = K_{anox} * N_{sw} * f_{anox} \quad [3]$$

$$J_{other} = K_{other} * N_{sw} * (1 - f_{anox}) \quad [4]$$

where f_{anox} is the fraction of seafloor impacted by bottom water anoxia, and K_{anox} and K_{other} are rate constants calculated for the modern uranium system. We assume a constant K_{anox}, reflecting similar mechanisms of U reduction at the sediment–water interface (SWI) throughout the studied time intervals. Similarly, K_{other} is also assumed to be constant. The concentration of uranium in carbonates is estimated by converting the moles of U in the seawater reservoir, N_{sw}, and assuming constant seawater calcium concentrations and a distribution coefficient of 1.4 (38). The sensitivity of the model to varying [Ca] is evaluated in *Uranium Biogeochemical Cycling and Model Sensitivity*. The model was first evaluated with parameters for the modern ocean, and then the $\delta^{238}U_{riv}$ term was adjusted to −0.05‰ to reflect a steady-state baseline value equal to the average Late Permian–Middle/Late Triassic seawater value as inferred from our data (*Middle Trassic $\delta^{238}U$ Composition*). A detailed description of the uranium cycle is provided in *Uranium Biogeochemical Cycling and Model Sensitivity*, and additional box model results are presented in Fig. S6. An evaluation of model sensitivity is presented in *Uranium Biogeochemical Cycling and Model Sensitivity* and in Fig. S9. R code used in our analysis can be accessed at https://purl.stanford.edu/mr858ss1453.

To determine the [U] and δ^{238}U relationships with f_{anox} shown in Fig. 3, we assume steady-state behavior and solve Eqs. **1** and **2** for N_{sw} and $\delta^{238}U$, respectively, as a function of f_{anox},

$$N_{sw} = \frac{J_{riv}}{K_{anox} * f_{anox} + K_{other} * (1 - f_{anox})} \quad [5]$$

$$\delta^{238}U = \delta^{238}U_{riv} - \frac{N_{sw} * [K_{other} * \Delta_{other} + f_{anox} * (K_{anox} * \Delta_{anox} - K_{other} * \Delta_{other})]}{J_{riv}}. \quad [6]$$

Geologic Setting. Our sample set includes three stratigraphic sections from the GBG, south China, and one stratigraphic section from the Aladag Nappe, Turkey (Fig. S1). Three of these sections were so shallow as to be oxygenated even if deeper waters (>100 m) were anoxic, and thus are less likely to have been impacted by diagenesis resulting from local redox conditions. From the GBG, we analyzed a suite of 86 samples for [U] and 55 samples for δ^{238}U from Dajiang and 32 samples for [U] and δ^{238}U from Guandao. We also analyzed three samples from the Dawen section, allowing us to compare our measured values across the Permian–Triassic boundary interval to those reported previously in a high-resolution δ^{238}U and Th/U record for the 15 m spanning the extinction horizon at the same site (11). To determine whether variations in [U] and δ^{238}U are globally reproducible, we also analyzed a suite of 36 samples for [U] and 31 samples from Taşkent, the Aladag Nappe, Turkey. We correlate the Taşkent section to the GBG using lithostratigraphy, conodont and foraminiferan biostratigraphy, and δ^{13}C chemostratigraphy (4, 20, 42). Detailed description of the stratigraphic sections is provided in *SI Materials and Methods* (Figs. S2–S4).

Uranium Isotopic Analysis. At least 4 g of sample powder was digested using 0.25 N Optima HCl, determined to be the optimal dissolution procedure (see *SI Materials and Methods* and Fig. S10). A ^{238}U:^{236}U sample to spike ratio of 10:1 was used to maximize both the internal precision and the external reproducibility of the δ^{238}U measurements. Uranium was purified by a two-step ion exchange chromatography procedure using UTEVA resin (Eichrom), following procedures adapted from refs. 16, 43.

Uranium isotopic compositions were measured in the ICP-MS/TIMS Facility at Stanford University on a Nu Plasma multicollector-inductively coupled plasma mass spectrometer (MC-ICP-MS). The $^{238}U/^{235}U$ ratios were corrected using an exponential law for mass bias assuming the certified spike $^{233}U/^{236}U$ ratio of 1.01906 (44), followed by correction for contribution of ^{238}U from the spike. The $^{238}U/^{235}U$ ratios are reported relative to reference standard CRM-145 in standard delta notation. Internal precision (2 SE) of measurements of standards was typically 0.07‰. Average measurement reproducibility (2σ), assessed by replicate measurements of the same sample solution, is 0.11‰ ($n = 83$). Additionally, we processed four samples twice to evaluate external reproducibility, where one limestone sample had a reproducibility of <0.01‰ and three dolomitic samples had an average reproducibility of 0.4‰ (Dataset S1; discussed in *Diagenetic Alteration and Dolomitization*). We evaluated reference materials BCR-2 (Columbia River Basalt), HU-1 (Harwell Uraninite), CRM-129a, and an internal carbonate standard to track reproducibility and agreement with previously published values; a summary is provided in *Supporting Information* and Fig. S11. A full description of analytical methods is included in *Supporting Information*, and the data from this study are presented in Dataset S1.

ACKNOWLEDGMENTS. We thank Caroline Harris and Monique Foung for laboratory assistance and five anonymous reviewers of this and earlier versions for their constructive suggestions that improved the manuscript. This research was supported by National Science Foundation Continental Dynamics Grant EAR-0807475 (to J.L.P.) and funding from Shell International Exploration and Production and Saudi Aramco (J.L.P.), American Chemical Society Petroleum Research Fund Grants 53241-ND2 (to K.M.) and 52457-ND2 (to J.L.P.), and an Achievement Rewards for College Scientists (ARCS) Fellowship and assistance from the Stanford McGee Fund (to K.V.L.).

1. Payne JL, Clapham ME (2012) End-Permian mass extinction in the oceans: An ancient analog for the 21st century? *Annu Rev Earth Planet Sci* 41:89–111.
2. Chen Z-Q, Benton MJ (2012) The timing and pattern of biotic recovery following the end-Permian mass extinction. *Nat Geosci* 5:375–383.
3. Foster WJ, Twitchett RJ (2014) Functional diversity of marine ecosystems after the Late Permian mass extinction event. *Nat Geosci* 7:233–238.
4. Payne JL, et al. (2004) Large perturbations of the carbon cycle during recovery from the end-Permian extinction. *Science* 305(5683):506–509.
5. Song HY, et al. (2014) Early Triassic seawater sulfate drawdown. *Geochim Cosmochim Acta* 128:95–113.
6. Grice K, et al. (2005) Photic zone euxinia during the Permian-Triassic superanoxic event. *Science* 307(5710):706–709.
7. Wignall PB, Hallam A (1992) Anoxia as a cause of the Permian/Triassic mass extinction: Facies evidence from northern Italy and the western United States. *Palaeogeogr Palaeoclimatol Palaeoecol* 93(1-2):21–46.
8. Wignall PB, Twitchett RJ (1996) Oceanic anoxia and the end Permian mass extinction. *Science* 272(5265):1155–1158.
9. Hallam A (1991) Why was there a delayed radiation after the end-Paleozoic extinctions? *Hist Biol* 5:257–262.
10. Loope GR, Kump LR, Arthur MA (2013) Shallow water redox conditions from the Permian–Triassic boundary microbialite: The rare earth element and iodine geochemistry of carbonates from Turkey and South China. *Chem Geol* 351:195–208.
11. Brennecka GA, Herrmann AD, Algeo TJ, Anbar AD (2011) Rapid expansion of oceanic anoxia immediately before the end-Permian mass extinction. *Proc Natl Acad Sci USA* 108(43):17631–17634.
12. Wignall PB, et al. (2010) An 80 million year oceanic redox history from Permian to Jurassic pelagic sediments of the Mino-Tamba terrane, SW Japan, and the origin of four mass extinctions. *Global Planet Change* 71(1-2):109–123.
13. Song HJ, et al. (2012) Geochemical evidence from bio-apatite for multiple oceanic anoxic events during Permian-Triassic transition and the link with end-Permian extinction and recovery. *Earth Planet Sci Lett* 353-354:12–21.
14. Grasby SE, Beauchamp B, Embry A, Sanei H (2012) Recurrent Early Triassic ocean anoxia. *Geology* 41(2):175–178.
15. Weyer S, et al. (2008) Natural fractionation of $^{238}U/^{235}U$. *Geochim Cosmochim Acta* 72(2):345–359.
16. Stirling CH, Andersen MB, Potter E-K, Halliday AN (2007) Low-temperature isotopic fractionation of uranium. *Earth Planet Sci Lett* 264(1-2):208–225.
17. Andersen MB, et al. (2014) A modern framework for the interpretation of $^{238}U/^{235}U$ in studies of ancient ocean redox. *Earth Planet Sci Lett* 400:184–194.
18. Stylo M, et al. (2015) Uranium isotopes fingerprint biotic reduction. *Proc Natl Acad Sci USA* 112(18):5619–5624.
19. Payne JL, et al. (2007) Erosional truncation of uppermost Permian shallow-marine carbonates and implications for Permian-Triassic boundary events. *Geol Soc Am Bull* 119(7-8):771–784.
20. Meyer KM, Yu M, Jost AB, Kelley BM, Payne JL (2011) δ^{13}C evidence that high primary productivity delayed recovery from end-Permian mass extinction. *Earth Planet Sci Lett* 302(3-4):378–384.
21. Lehrmann DJ, et al. (2005) Permian-Triassic boundary and a Lower-Middle Triassic boundary sequence on the Great Bank of Guzihou, Nanpanjiang basin, southern Guizhou Province. *Albertiana* 33:169–186.
22. Song HY, et al. (2013) Large vertical $\delta^{13}C_{DIC}$ gradients in Early Triassic seas of the South China craton: Implications for oceanographic changes related to Siberian Traps volcanism. *Global Planet Change* 105:7–20.
23. Burgess SD, Bowring S, Shen SZ (2014) High-precision timeline for Earth's most severe extinction. *Proc Natl Acad Sci USA* 111(9):3316–3321.
24. Ovtcharova M, et al. (2006) New Early to Middle Triassic U–Pb ages from South China: Calibration with ammonoid biochronozones and implications for the timing of the Triassic biotic recovery. *Earth Planet Sci Lett* 243(3-4):463–475.
25. Schaal EK, Clapham ME, Rego BL, Wang SC, Payne JL (2016) Comparative size evolution of marine clades from the Late Permian through Middle Triassic. *Paleobiology* 42(01):127–142.

26. Ehrenberg SN, Svånå TA, Swart PK (2008) Uranium depletion across the Permian–Triassic boundary in Middle East carbonates: Signature of oceanic anoxia. *AAPG Bull* 92(6):691–707.
27. Tavakoli V, Rahimpour-Bonab H (2012) Uranium depletion across Permian–Triassic Boundary in Persian Gulf and its implications for paleooceanic conditions. *Palaeogeogr Palaeoclimatol Palaeoecol* 350-352:101–113.
28. Helly JJ, Levin LA (2004) Global distribution of naturally occurring marine hypoxia on continental margins. *Deep Sea Res Part I Oceanogr Res Pap* 51(9):1159–1168.
29. Algeo TJ, et al. (2010) Changes in productivity and redox conditions in the Panthalassic Ocean during the latest Permian. *Geology* 38(2):187–190.
30. Algeo TJ, et al. (2011) Spatial variation in sediment fluxes, redox conditions, and productivity in the Permian–Triassic Panthalassic Ocean. *Palaeogeogr Palaeoclimatol Palaeoecol* 308(1-2):65–83.
31. Winguth C, Winguth AME (2012) Simulating Permian-Triassic oceanic anoxia distribution: Implications for species extinction and recovery. *Geology* 40(2):127–130.
32. Luo G, et al. (2010) Isotopic evidence for an anomalously low oceanic sulfate concentration following end-Permian mass extinction. *Earth Planet Sci Lett* 300(1-2): 101–111.
33. Payne JL, Kump L (2007) Evidence for recurrent Early Triassic massive volcanism from quantitative interpretation of carbon isotope fluctuations. *Earth Planet Sci Lett* 256(1-2): 264–277.
34. Romaniello SJ, Herrmann AD, Anbar AD (2013) Uranium concentrations and $^{238}U/^{235}U$ isotope ratios in modern carbonates from the Bahamas: Assessing a novel paleoredox proxy. *Chem Geol* 362:305–316.
35. Dunk R, Mills R, Jenkins W (2002) A reevaluation of the oceanic uranium budget for the Holocene. *Chem Geol* 190(1-4):45–67.
36. Montoya-Pino C, et al. (2010) Global enhancement of ocean anoxia during Oceanic Anoxic Event 2: A quantitative approach using U isotopes. *Geology* 38(4):315–318.
37. Morford JL, Emerson S (1999) The geochemistry of redox sensitive trace metals in sediments. *Geochim Cosmochim Acta* 63(11/12):1735–1750.
38. Maher K, Steefel CI, DePaolo DJ, Viani BE (2006) The mineral dissolution rate conundrum: Insights from reactive transport modeling of U isotopes and pore fluid chemistry in marine sediments. *Geochim Cosmochim Acta* 70(2):337–363.
39. Noordmann J, Weyer S, Georg RB, Jöns S, Sharma M (2015) $^{238}U/^{235}U$ isotope ratios of crustal material, rivers and products of hydrothermal alteration: New insights on the oceanic U isotope mass balance. *Isotopes Environ Health Stud* 18:1–23.
40. Tissot FLH, Dauphas N (2015) Uranium isotopic compositions of the crust and ocean: Age corrections, U budget and global extent of modern anoxia. *Geochim Cosmochim Acta* 167:113–143.
41. Andersen MB, et al. (2016) Closing in on the marine $^{238}U/^{235}U$ budget. *Chem Geol* 420: 11–22.
42. Lehrmann DJ (1998) Controls on facies architecture of a large Triassic carbonate platform: The Great Bank of Guizhou, Nanpanjiang Basin, south China. *J Sediment Res* 68(2):311–326.
43. Potter E-K, Stirling CH, Andersen MB, Halliday AN (2005) High precision Faraday collector MC-ICPMS thorium isotope ratio determination. *Int J Mass Spectrom* 247(1-3):10–17.
44. Richter S, et al. (2008) The isotopic composition of natural uranium samples—Measurements using the new $n(^{233}U)/n(^{236}U)$ double spike IRMM-3636. *Int J Mass Spectrom* 269(1-2):145–148.
45. Lehrmann DJ, et al. (2015) An integrated biostratigraphy (conodonts and foraminifers) and chronostratigraphy (paleomagnetic reversals, magnetic susceptibility, elemental chemistry, carbon isotopes and geochronology) for the Permian–Upper Triassic strata of Guandao section, Nanpanjiang Basin, south China. *J Asian Earth Sci* 108:117–135.
46. Payne JL, et al. (2010) Calcium isotope constraints on the end-Permian mass extinction. *Proc Natl Acad Sci USA* 107(19):8543–8548.
47. Altiner D, Özgül N (2001) Carboniferous and Permian of the allochthonous terranes of the Central Tauride Belt, southern Turkey. *PaleoForams 2001, International Conference on Paleozoic Benthic Foraminifera Guidebook*, (Middle East Tech Univ, Ankara, Turkey), p 35.
48. Özgül N (1997) Stratigraphy of the tectono-stratigraphic units in the region Bozkir-Hadim-Taşkent (northern central Taurides). *Miner Res Explor Inst Turkey Bull* 119: 113–174. Turkish with English abstract.
49. Monod O (1977) Recherches géologiques dans le Taurus occidental au Sud de Beysehir (Turquie) PhD thesis (Université de Paris-Sud, Orsay, France).
50. Brand U, Veizer J (1980) Chemical diagenesis of a multicomponent carbonate system–1: Trace elements. *J Sediment Petrol* 50(4):1219–1236.
51. Condon DJ, McLean N, Noble SR, Bowring SA (2010) Isotopic composition ($^{238}U/^{235}U$) of some commonly used uranium reference materials. *Geochim Cosmochim Acta* 74(24):7127–7143.
52. Cheng H, et al. (2013) Improvements in ^{230}Th dating, ^{230}Th and ^{234}U half-life values, and U–Th isotopic measurements by multi-collector inductively coupled plasma mass spectrometry. *Earth Planet Sci Lett* 371-372:82–91.
53. Brennecka GA, Wasylenki LE, Bargar JR, Weyer S, Anbar AD (2011) Uranium isotope fractionation during adsorption to Mn-oxyhydroxides. *Environ Sci Technol* 45(4):1370–1375.
54. Kendall B, Brennecka GA, Weyer S, Anbar AD (2013) Uranium isotope fractionation suggests oxidative uranium mobilization at 2.50Ga. *Chem Geol* 362:105–114.
55. Maher K, Bargar JR, Brown GE, Jr (2013) Environmental speciation of actinides. *Inorg Chem* 52(7):3510–3532.
56. Langmuir D (1978) Uranium solution-mineral equilibria at low temperatures with applications to sedimentary ore deposits. *Geochim Cosmochim Acta* 42(6A):547–569.
57. Ku T-L, Knauss KG, Mathieu GG (1977) Uranium in open ocean: Concentration and isotopic composition. *Deep Sea Res* 24(11):1005–1017.
58. Holmden C, Amini M, Francois R (2015) Uranium isotope fractionation in Saanich Inlet: A modern analog study of a paleoredox tracer. *Geochim Cosmochim Acta* 153: 202–215.
59. Basu A, Sanford RA, Johnson TM, Lundstrom CC, Löffler FE (2014) Uranium isotopic fractionation factors during U(VI) reduction by bacterial isolates. *Geochim Cosmochim Acta* 136:100–113.
60. Stirling CH, Andersen MB, Warthmann R, Halliday AN (2015) Isotope fractionation of ^{238}U and ^{235}U during biologically-mediated uranium reduction. *Geochim Cosmochim Acta* 163:200–218.
61. Goto KT, et al. (2014) Uranium isotope systematics of ferromanganese crusts in the Pacific Ocean: Implications for the marine $^{238}U/^{235}U$ isotope system. *Geochim Cosmochim Acta* 146:43–58.
62. Anderson RF, Fleisher MQ, LeHuray AP (1989) Concentration, oxidation state, and particulate flux of uranium in the Black Sea. *Geochim Cosmochim Acta* 53(9): 2215–2224.
63. Hua B, Xu H, Terry J, Deng B (2006) Kinetics of uranium(VI) reduction by hydrogen sulfide in anoxic aqueous systems. *Environ Sci Technol* 40(15):4666–4671.
64. Stewart BD, Neiss J, Fendorf S (2007) Quantifying constraints imposed by calcium and iron on bacterial reduction of uranium(VI). *J Environ Qual* 36(2):363–372.
65. Bluth GJS, Kump LR (1991) Phanerozoic paleogeology. *Am J Sci* 291:284–308.
66. Meece DE, Benninger LK (1993) The coprecipitation of Pu and other radionuclides with $CaCO_3$. *Geochim Cosmochim Acta* 57(7):1447–1458.
67. Reeder RJ, Nugent M, Lamble GM, Drew Tait C, Morris DE (2000) Uranyl incorporation into calcite and aragonite: XAFS and luminescence studies. *Environ Sci Technol* 34(4): 638–644.
68. DeCarlo TM, Gaetani GA, Holcomb M, Cohen AL (2015) Experimental determination of factors controlling U/Ca of aragonite precipitated from seawater: Implications for interpreting coral skeleton. *Geochim Cosmochim Acta* 162:151–165.
69. Woods AD, Bottjer DJ, Mutti M, Morrison J (1999) Lower Triassic large sea-floor carbonate cements: Their origin and a mechanism for the prolonged biotic recovery from the end-Permian mass extinction. *Geology* 27(7):645–648.
70. Pruss SB, Bottjer DJ, Corsetti FA, Baud A (2006) A global marine sedimentary response to the end-Permian mass extinction: Examples from southern Turkey and the western United States. *Earth Sci Rev* 78(3-4):193–206.
71. Isozaki Y (1997) Permo-Triassic boundary superanoxia and stratified superocean: Records from lost deep sea. *Science* 276(5310):235–238.
72. Payne JL, Lehrmann DJ, Christensen S, Wei J, Knoll AH (2006) Environmental and biological controls on the initiation and growth of a Middle Triassic (Anisian) reef complex on the Great Bank of Guizhou, Guizhou Province, China. *Palaios* 21(4): 325–343.
73. Morford JL, Martin WR, Carney CM (2009) Uranium diagenesis in sediments underlying bottom waters with high oxygen content. *Geochim Cosmochim Acta* 73(10): 2920–2937.
74. McManus J, Berelson WM, Klinkhammer GP, Hammond DE, Holm C (2005) Authigenic uranium: Relationship to oxygen penetration depth and organic carbon rain. *Geochim Cosmochim Acta* 69(1):95–108.
75. Shen J, et al. (2012) Volcanic perturbations of the marine environment in South China preceding the latest Permian mass extinction and their biotic effects. *Geobiology* 10(1):82–103.
76. Stanley SM, Hardie LA (1998) Secular oscillations in the carbonate mineralogy of reef-building and sediment-producing organisms driven by tectonically forced shifts in seawater chemistry. *Palaeogeogr Palaeoclimatol Palaeoecol* 144(1-2):3–19.
77. Payne JL, Lehrmann DJ, Wei J, Knoll AH (2006) The pattern and timing of biotic recovery from the end-Permian extinction on the Great Bank of Guizhou, Guizhou Province, China. *Palaios* 21(1):63–85.
78. Team RDC (2008) *R: A Language and Environment for Statistical Computing* (R Found Stat Comput, Vienna).
79. Brennecka GA, Borg LE, Hutcheon ID, Sharp MA, Anbar AD (2010) Natural variations in uranium isotope ratios of uranium ore concentrates: Understanding the $^{238}U/^{235}U$ fractionation mechanism. *Earth Planet Sci Lett* 291(1-4):228–233.
80. Sedlacek ARC, et al. (2014) $^{87}Sr/^{86}Sr$ stratigraphy from the Early Triassic of Zal, Iran: Linking temperature to weathering rates and the tempo of ecosystem recovery. *Geology* 42(9):779–782.
81. Korte C, Kozur HW, Bruckschen P, Veizer J (2003) Strontium isotope evolution of Late Permian and Triassic seawater. *Geochim Cosmochim Acta* 67(1):47–62.
82. Brasier MD, Lindsay JF (2000) Did supercontinental amalgamation trigger the "Cambrian Explosion"? *The Ecology of the Cambrian Radiation*, eds Zhuravlev AY, Riding R (Columbia Univ Press, New York), pp 69–89.
83. Jenkyns HC, Gale AS, Corfield RM (1994) Carbon- and oxygen-isotope stratigraphy of the English Chalk and Italian Scaglia and its palaeoclimatic significance. *Geol Mag* 131(1):1–34.
84. Saltzman MR, Edwards CT, Adrain JM, Westrop SR (2015) Persistent oceanic anoxia and elevated extinction rates separate the Cambrian and Ordovician radiations. *Geology* 43(9):807–810.
85. Ingall ED, Bustin RM, Van Cappellen P (1993) Influence of water column anoxia on the burial and preservation of carbon and phosphorus in marine shales. *Geochim Cosmochim Acta* 57(2):303–316.
86. Van Cappellen P, Ingall ED (1996) Redox stabilization of the atmosphere and oceans by phosphorus-limited marine productivity. *Science* 271:493–496.
87. Lavigne H, Epitalon J-M, & Gattuso J-P (2014) seacarb: seawater carbonate chemistry with R (R package version 3.0). Available at CRAN.R-project.org/package=seacarb.